This article has been accepted for publication in a future issue of this journal, but has not been fully edited. Content may change prior to final publication. Citation information: DOI 10.1109/TPEL.2021.3127010, IEEE Transactions on Power Electronics

IEEE POWER ELECTRONICS REGULAR PAPER

A Single-Stage Electrolytic Capacitor-less EV Charger with Single- and Three-Phase Compatibility

Hyungjin Kim, Junyeong Park, Sunju Kim, Ramadhan Muhammad Hakim, Hamza Belkamel, and Sewan Choi, *Fellow*, *IEEE*

***Abstract*- This paper proposes a modular single-stage electrolytic capacitor-less EV charger with single and three-phase grid compatibility. The proposed single-stage structure inherently maintains DC charging current for three-phase grid. For single-phase grid, a phase module is reconfigured to operate as a power decoupling circuit, making battery current to be DC. Furthermore, the proposed single-stage OBC is able to achieve zero voltage switching (ZVS) under wide grid and battery voltage ranges with only one control variable of phase shift angle. A balancing control method is proposed to ensure pure DC battery charging under unbalanced grid conditions. An optimized design of the planar core with Litz wire for achieving low profile is presented. Finally, a 11 kW prototype of the proposed charger achieved a power density of 5.25 kW/L and demonstrated 97.01% peak efficiency.**

***Index Terms* –On-board charger, three-phase charger, universal charger, electrolytic capacitor-less, power decoupling circuit, single-stage, planar core, high power density, 800V battery.**

I. Introduction

In the past two decades, electric vehicles (EVs) have emerged as a viable alternative to internal combustion engine vehicles to reduce greenhouse gas emissions. Despite being environment friendly, limited driving range and long battery charging time are two major obstacles to increase customer acceptance for EV. Therefore, a high capacity battery is required to reduce the range anxiety. However, high capacity battery implies a long charging time. Accordingly, the power level of the on-board charger (OBC) is required to increase for shortening the charging time. While increasing the charging power, some requirements need to be considered in the design of OBCs as set by the U.S. Department of Energy (DoE) [1]. As illustrated in Table I, the power density of the OBC is of great importance due to the limited space in the EV. Additionally, the efficiency of OBC has significant impact on the charging time and the battery recharging fee. Notably, owing to lower operating cost, EVs will be widely used in Mobility-as-a-Service (MaaS) applications such as car-share and connected-taxi where long operating time (50,000 to 80,000 miles a year) and high reliability are required [1]. Therefore, in 2025 the OBC reliability has to reach 300,000 miles [1]. It is worthy to mention that the presence of electrolytic capacitors in OBC threatens system reliability [2]. In addition, the electrolytic capacitor increases overall volume of the OBC due to high profile.

Up to now, the single-phase OBC has been commonly used due to the availability of single-phase grid worldwide. The single-phase grid enables the overnight charging of EV at private facilities where only single-phase outlets are available [3]. As another option, the three-phase grid offers higher charging power, and therefore reduces the charging time. Thus, EVs equipped with three-phase OBCs are increasing especially in the European market since the charging infrastructure is dominated by three-phase grid in many European countries [4], [5]. Hence, it is commercially valuable to design universal OBCs that are compatible with both single- and three-phase grid for worldwide use [6]. The universal OBCs can be used at both public points and home [5]. Fig. 1 shows the electrical specifications of on-board charging in major countries.

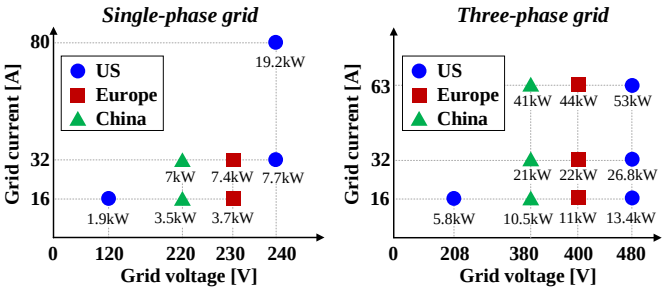

Fig. 1. Electrical specifications of on-board charging in major countries.

TABLE I
U.S. DoE Targets For On-Board Charger [1]

Target year	Power density [kW/L]	Efficiency [%]	Reliability [mile]	Cost [$/kW]
2020	3.5	97	150k (5 years)	50
2025	4.6	98	300k (5 years)	35

The commercially available OBCs are the two-stage structure that consists of a power factor correction (PFC) stage and an isolated DC-DC stage with DC-link electrolytic capacitors [7]-[16]. This topology can be easily modular for single- and three-phase compatibility. However, there are limitations in improving efficiency due to double power conversion and increasing power density because of high component count. Moreover, DC-link electrolytic capacitors decrease the system reliability due to their short life-time.

The non-modular two-stage structure was considered for three-phase grid [17]-[19]. This structure has a lower component count compared to the aforementioned modular two-stage structure. However, in order to be compatible with single- and three-phase grid, a significant number of electrolytic capacitors should be used for this structure due to simultaneous requirement of large capacitance with voltage rating of 400 V for single-phase grid and small capacitance with high voltage

This work was supported by the National Research Foundation of Korea (NRF) grant funded by the Korea government (MSIT). (No. 2020R1A2C2006301)

This article has been accepted for publication in a future issue of this journal, but has not been fully edited. Content may change prior to final publication. Citation information: DOI 10.1109/TPEL.2021.3127010, IEEE Transactions on Power Electronics

rating of 800 V for three-phase grid [6]. In this case, the required DC-link capacitor is realized with series and parallel connection of 400 V electrolytic capacitors, resulting in four times larger volume compared to its modular counterpart [6].

In this regard, some topologies to eliminate the electrolytic capacitor have been introduced [20]-[35]. The 22 kW non-modular two-stage OBC in [20] that is compatible with single- and three-phase grid has DC charging capability without using bulky electrolytic capacitors, achieving power density of 2.04 kW/L. For single-phase, the second harmonic current is absorbed by an integrated power decoupling circuit (IPDC) with a small decoupling capacitance of 150 μF. The obtained peak efficiency is 94% due to double power conversion.

In another way, the single-stage OBC has been considered to possibly achieve high efficiency and high power density due to its simple structure and low component count [23]-[35]. In order to be realizable as a single- and three-phase compatible OBC, the single-stage topology should be able to deal with the second-harmonic component efficiently in terms of cost and volume. Moreover, achieving soft-switching of the single-stage OBC while maintaining high efficiency under wide voltage range is challenging. In [23]-[26] single-phase OBCs based on indirect matrix converter were introduced. High power density was achieved since bulky electrolytic capacitors are eliminated while allowing the second-harmonic current to flow in the battery. Therefore, for DC charging current, additional power decoupling circuits are required to absorb the second-harmonic current.

In particular, the modular three-phase single-stage structure proposed in [32] provides DC charging current. It achieves high power density of 3.3 kW/L and high efficiency of greater than 97% using GaN devices. However, an external power decoupling circuit is required to absorb the second-harmonic for single-phase grid [25], [26]. Further, in order to achieve ZVS over wide grid and battery voltage ranges, this method uses four control variables including three phase-shift angles and switching frequency, making the implemented controller complex.

This paper proposes a modular single-stage electrolytic capacitor-less OBC that is compatible with single and three-phase grid, where each module is constructed based on the topology presented in [27], [42], [43]. For three-phase grid, DC charging current is inherently maintained due to three output currents with 120-degrees phase shift to each other. Also, in order to provide DC battery charging current for single-phase grid, the power decoupling circuit is configured by utilizing a phase module, which does not necessitate additional circuit except a relay and a decoupling capacitor. Furthermore, the proposed single-stage OBC is able to achieve ZVS under wide grid and battery voltage ranges with only one control variable of phase shift angle.

II. Proposed Single- and Three-Phase Compatible EV Charger

Fig. 2 shows the conceptual structure of the proposed single- and three-phase compatible EV charger for single and three phase DC charging. The proposed charger is constructed using three single-stage electrolytic-capacitor-less high frequency isolated AC-DC converters. For three-phase charging, the three modules are output parallel-connected. Each module processes 3.7 kW. Therefore, the three-phase charger is capable of delivering power up to 11 kW. As shown in Fig. 2(a), three relays are used to switch between three- and single- phase charging modes. In the three-phase mode, *Relay* 2 is closed as depicted in Fig. 2(b). In single-phase mode shown in Fig. 2(c), *Relay* 1 is closed to enable the parallel input connection of *Module A* and *Module B* (input current sharing), whereas *Module C* is disconnected from the grid by opening *Relay* 2, connected to a decoupling capacitor C_{pd} through *Relay* 3, and operates as an integrated power decoupling circuit to absorb the second-harmonic ripple power in the single-phase mode. Hence,

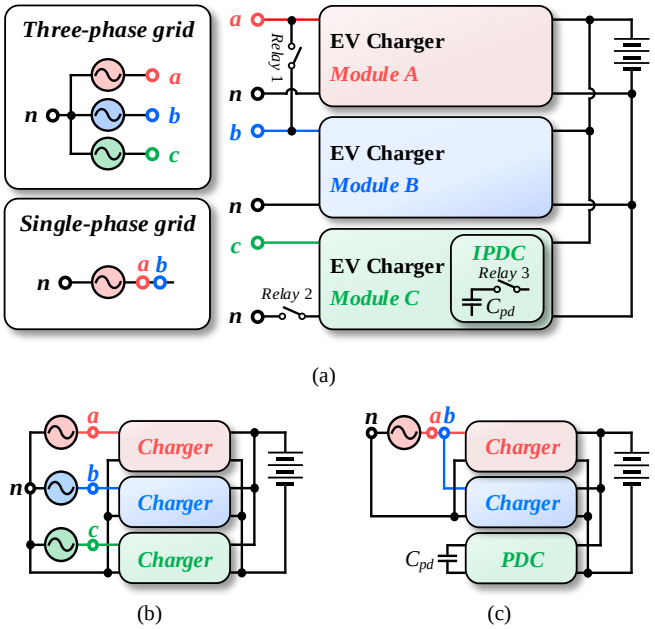

Fig. 2. Conceptual structure of the proposed single- and three-phase compatible EV charger with integrated power decoupling circuit. (a) Whole structure. (b) Three-phase structure. (c) Single-phase structure.

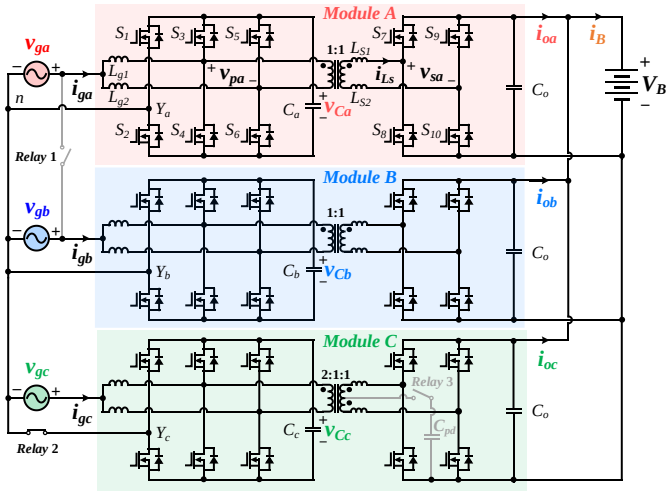

Fig. 3. Circuit configuration of the proposed EV charger for three-phase grid.

This article has been accepted for publication in a future issue of this journal, but has not been fully edited. Content may change prior to final publication. Citation information: DOI 10.1109/TPEL.2021.3127010, IEEE Transactions on Power Electronics

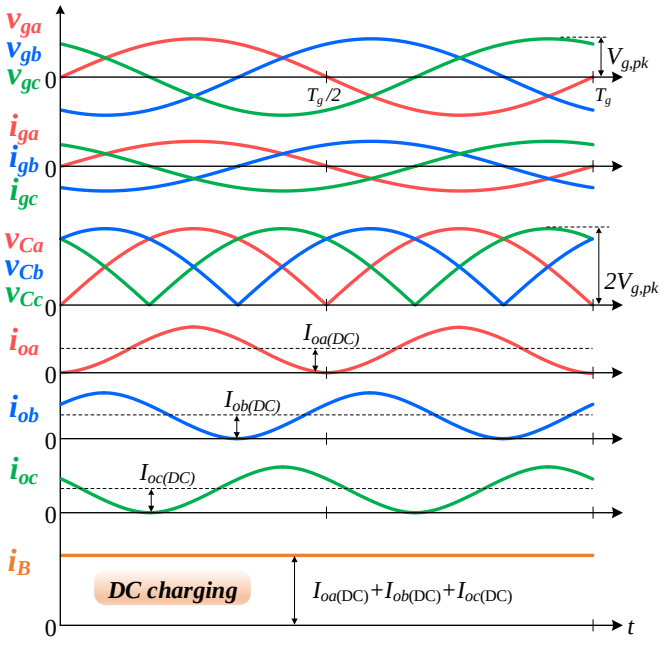

Fig. 4. Key waveforms of the proposed EV charger for three-phase grid.

it is possible to provide dc battery charging up to 7.4 kW with single-phase grid.

A. Operating principles for three-phase grid connection

Fig. 3 shows the circuit configuration of the proposed EV charger for three-phase grid. The proposed three-phase structure is composed of three single-phase modules introduced in [27], [42], [43] where each module is the single-stage interleaved totem-pole electrolytic capacitor-less AC-DC converter. In the three-phase charging mode, the three modules are connected to a three-phase four wire grid, where the common points $Y_{(a, b, c)}$ of the modules (A, B, C) are connected to the grid neutral point n. Hence, the three single-phase modules (A, B, C) operate independently from each other with their input voltages equal to the respective phase-to-neutral voltages of the grid. The inductors L_S are the power transfer element where L_s represents the total inductance including external inductors and leakage inductance of the HF transformer, where L_{S1}=L_{S2}. Small film capacitors $C_{(a,b,c)}$ are used to clamp voltage spikes caused by the leakage inductances of the transformers.

In the three-phase charging mode, the instantaneous powers at the grid side and at the DC-side of each module are identical since the module does not have any energy storage for storing the second harmonic power. Therefore, the output currents of each module are 120° out of phase and mainly include dc and second-harmonic components, as shown in Fig. 4. Since the operation of the three modules is the same, the sum of the three output currents results in pure DC battery current i_B.

Fig. 5 shows the operating waveforms of a single module for positive half-line cycle. S_1 and S_2 are line-frequency (50 Hz/60 Hz) switches and form a low-frequency synchronous rectifier bridge. The two interleaving legs consisting of S_3~S_6 are 180° out of phase and switched in diagonal manner with a fixed 50% duty (d_p). Hence, the voltage across the clamping film capacitor is twice the rectified grid voltage ($v_{C(a,b,c)}$=2|v_g|).

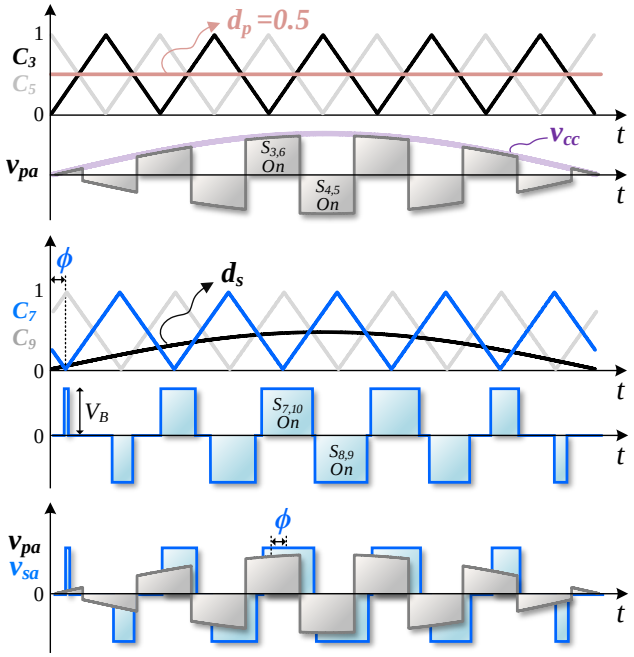

Fig. 5. Operating waveforms of a single module for the positive half-line cycle.

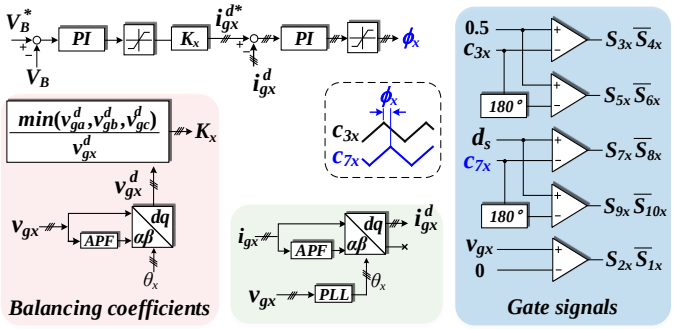

Fig. 6. Control block diagram of the proposed EV charger for balancing phase power and maintaining pure DC charging current under unbalanced grid voltage (x = a, b, c).

Note that the voltage v_{pa} across the AC-side of the transformer having a sinusoidal envelope is low-frequency-component-free.

The two legs of the full-bridge at the battery side are 180° phase-shifted and modulated using the signal $d_s(t) = 0.5|\sin(\omega_g t)|$. As a result, the secondary-side voltage v_{sa} of the transformer has a three-level waveform. The power delivered by each module is controlled based on the phase shift between v_{pa} and v_{sa}, as illustrated in Fig. 5.

Fig. 6 shows the control block diagram of the proposed EV charger for balancing phase power under unbalanced grid voltage. The main objective of the control system is to ensure pure DC battery charging without low frequency component under unbalanced as well as balanced grid conditions.

The control system comprises an outer-loop DC voltage controller and inner-loop current controller. The voltage PI controller integrates the error between the pure DC feedback voltage and reference DC voltage to generate the corresponding reference grid current. The inner PI current controllers determine the phase angles of the shifted carriers (C_{7x}) with

This article has been accepted for publication in a future issue of this journal, but has not been fully edited. Content may change prior to final publication. Citation information: DOI 10.1109/TPEL.2021.3127010, IEEE Transactions on Power Electronics

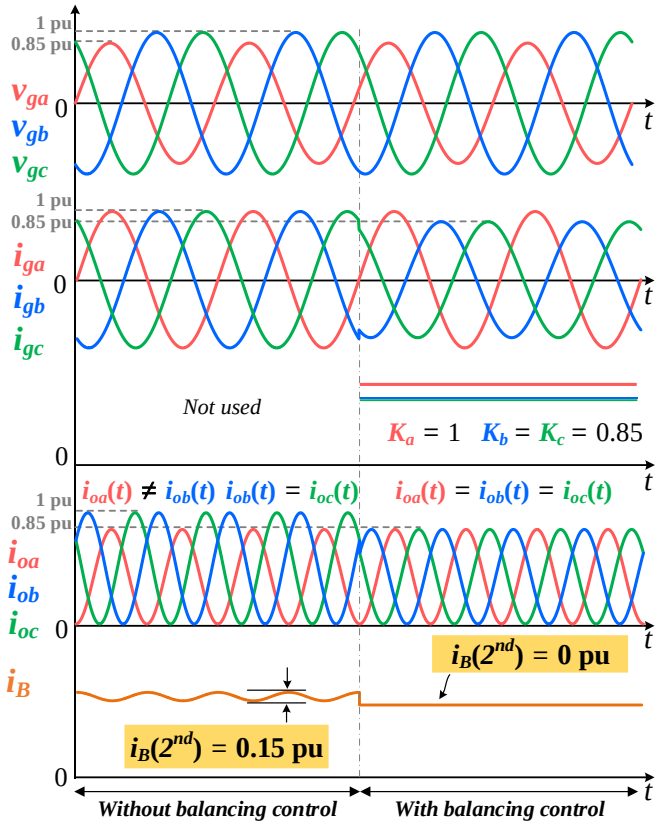

Fig. 7. Battery current under unbalanced voltage sag (v_{ga} = 0.85 pu).

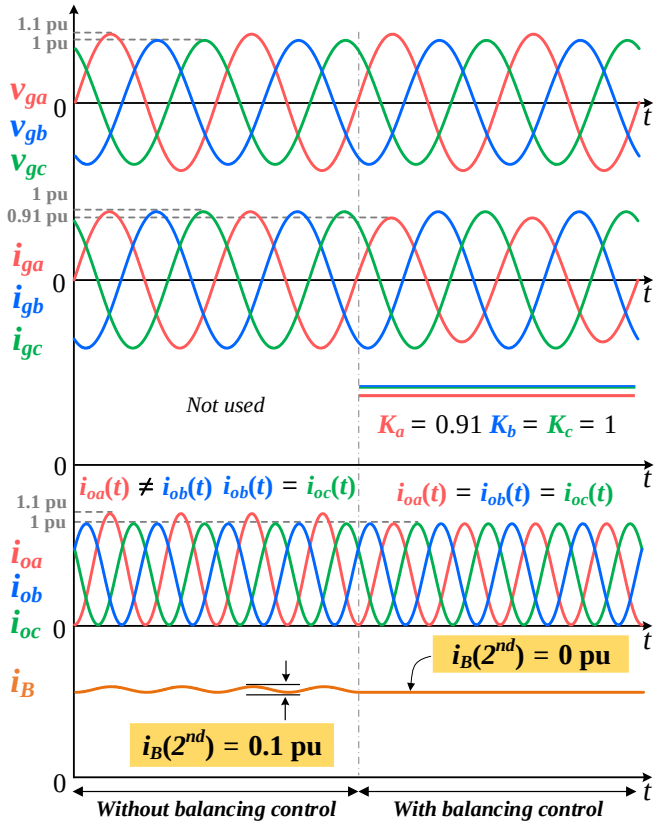

Fig. 8. Battery current under unbalanced voltage swell (v_{ga} = 1.1 pu).

respect to reference carrier signal of each phase (C_{3x}). Moreover, three balancing coefficients are introduced in the control block to ensure pure DC charging battery current regardless of the grid conditions (sag/swell) without exceeding component current ratings.

For the case of balanced three-phase grid voltage as shown in Fig. 4, the three balancing coefficients are equal to 1. Therefore, the control is the same as the dual-loop controller, and identical power is delivered by each phase module ($i_{oa}(t)$= $i_{ob}(t)$=$i_{oc}(t)$). Fig.7 (8) shows the case of unbalanced voltage sag (swell) where phase '*a*' is dropped (increased) by 15% (10%). Without the proposed balancing control, phase '*a*' delivers lower (higher) power compared to the other two phases, resulting in battery current with the second-harmonic ripple.

With the balancing control, coefficients K_x determined by the equation in Fig. 6 are introduced to maintain identical power in the three modules, thereby eliminating the second-harmonic ripple and ensuring a pure DC charging current. For the phase with the lowest peak voltage among v_{gx}^{d}, the balancing coefficient is equal to 1 while for the other phases with higher peak voltage the balancing coefficients become smaller than 1. It is noted that balancing coefficients K_x are always less than or equal to 1.

B. Operating principles for single-phase grid connection

The circuit configuration of the proposed EV charger for single-phase grid is shown in Fig. 9. The single-phase grid can be connected to a single module or two modules according to the battery charging profile (constant current (CC) / constant voltage (CV) mode); During the CC mode where the power is usually greater than 3.7 kW, *Module A* and *Module B* are parallel-input parallel-output connected by closing *Relay* 1. During the CV mode where the power goes usually under 3.7 kW, by opening *Relay* 1, only *Module A* is operated to increase the system efficiency. Fig. 10 shows the key waveforms of the proposed EV charger for single-phase grid at the power levels greater than 3.7 kW.

Since *Module A* and *Module B* are connected to the common grid voltage, they have same voltage waveforms across the clamping capacitors, and their output current waveforms are also identical, as shown in Fig. 10. The resulting output current i_{oa}+i_{ob} mainly includes DC component and large second-harmonic component. In order to remove the second-harmonic component in the battery current, *Module C* is reconfigured to behave as a power decoupling circuit by opening *Relay* 2 and closing *Relay* 3, which connects decoupling capacitor C_{pd}. The primary-side of the transformer is shorted by turning on the two bottom switches (S_4 and S_6) in *Module C*. Hence, as shown in Fig. 11(a) the impedance seen from the secondary-side of the transformer is zero, thereby deactivating the transformer in *Module C*. Finally, the power decoupling circuit is nothing but a two-phase interleaved buck converter, as shown in Fig. 11(b). Since L_{S1} and L_{S2} are significantly small inductances, the interleaved buck converter operates in discontinuous conduction mode (DCM). It is noted that *Module A* and *Module B* can be seen as a current

This article has been accepted for publication in a future issue of this journal, but has not been fully edited. Content may change prior to final publication. Citation information: DOI 10.1109/TPEL.2021.3127010, IEEE Transactions on Power Electronics

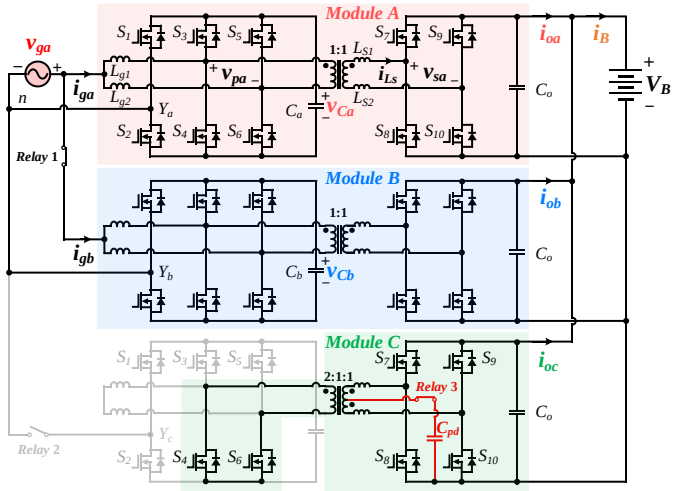

Fig. 9. Circuit configuration of the proposed EV charger for single-phase grid.

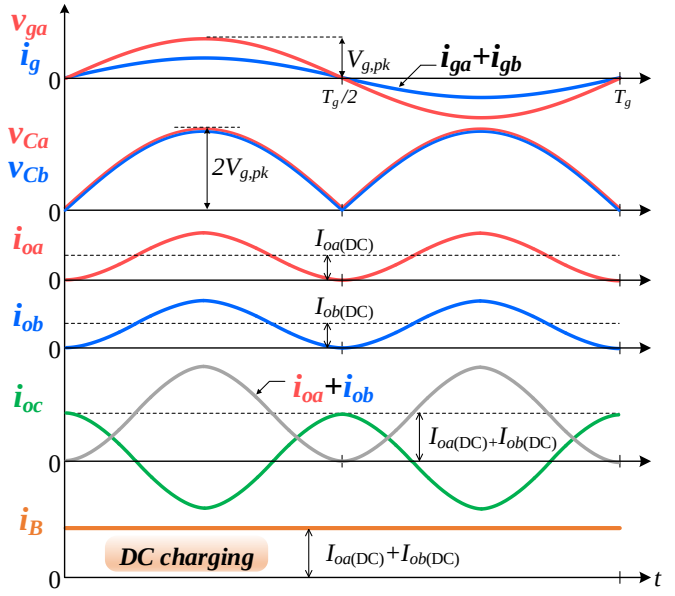

Fig. 10. Key waveforms of the proposed EV charger for a single-phase grid.

source with a value of $i_{oa}+i_{ob}$ that contains the DC and second-harmonic components, as shown in Fig. 11.

Fig. 12 shows a control block diagram of the proposed EV charger for maintaining pure DC charging current under single-phase grid. *Module A* and *B* provide charging power for the battery and *Module C* operates as the integrated power decoupling circuit to absorb low-frequency component. In power decoupling control, a band pass filter (BPF) that has the center frequency at 100/120 Hz is employed in order to extract the double-line-frequency component from the battery current. The proportional-resonant (PR) controller regulates the magnitude of the second harmonic component in $i_{oa}+i_{ob}$ toward zero. Hence, the two-phase interleaved buck converter is switched to divert the second-ripple power to the decoupling capacitor. The interleaved effect with balanced current is achieved without independent current sensing of each phase due to DCM operation [36].

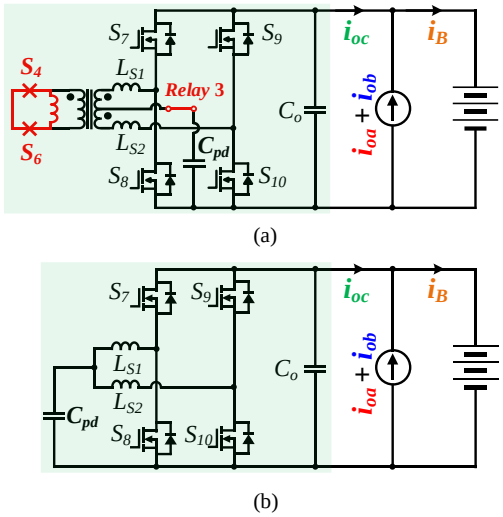

Fig. 11. Integrated power decoupling circuit for single-phase DC charging. (a) Configuration of the power decoupling circuit. (b) Equivalent power decoupling circuit.

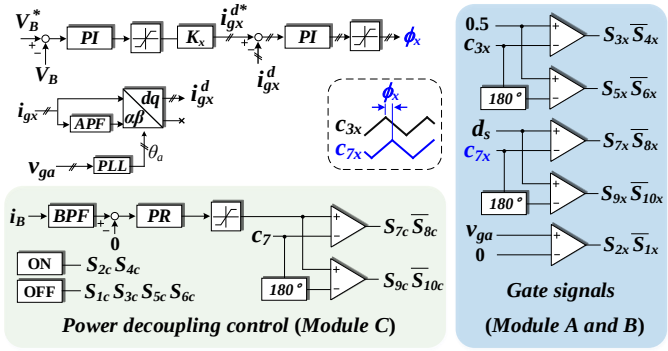

Fig. 12. Control block diagram of the proposed EV charger for maintaining pure DC charging current under single-phase grid (x= a, b).

III. Optimized Planar Transformer Design

To achieve high power density, the design of magnetic components with low profile is essential. Two types of winding structures can be implemented: Litz wire and PCB winding. In OBC applications, limited switching frequency operation leads to a high applied volt-second across the transformer terminal. In this case, more winding turns are required to avoid saturation and minimize the maximum flux density. Implementing many turns with PCB winding may cause high DC resistance due to its low fill factor characteristic [37], [38]. Moreover, the high stray capacitance of PCB winding may cause unwanted resonance that leads to waveform distortion [39]. On the other hand, the Litz wire offers a better fill factor and lower winding stray capacitance compared to the PCB winding structure. However, the Litz wire structure may not be suitable at higher frequencies where the eddy current starts to dominate the overall winding loss.

Considering the characteristics of Litz wire and PCB winding, it is necessary to make a comparison so that the most suitable structure for the planar transformer with the given specifications can be selected. In this section, a comparison between PCB winding and Litz wire in terms of winding loss,

This article has been accepted for publication in a future issue of this journal, but has not been fully edited. Content may change prior to final publication. Citation information: DOI 10.1109/TPEL.2021.3127010, IEEE Transactions on Power Electronics

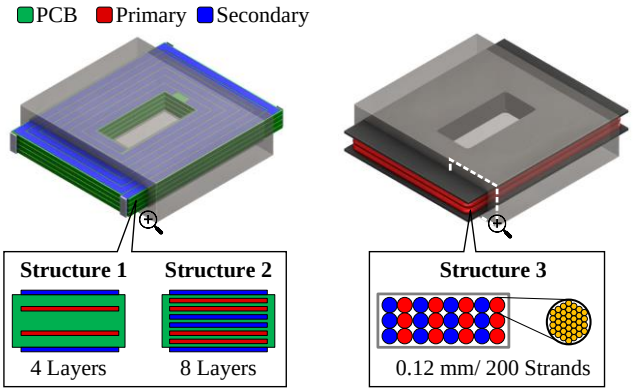

Fig. 13. Planar transformer winding structures. (a) PCB winding structures and layer arrangement for 4 layers (Structure 1) and 8 layers (Structure 2). (b) Litz wire winding (Structure 3).

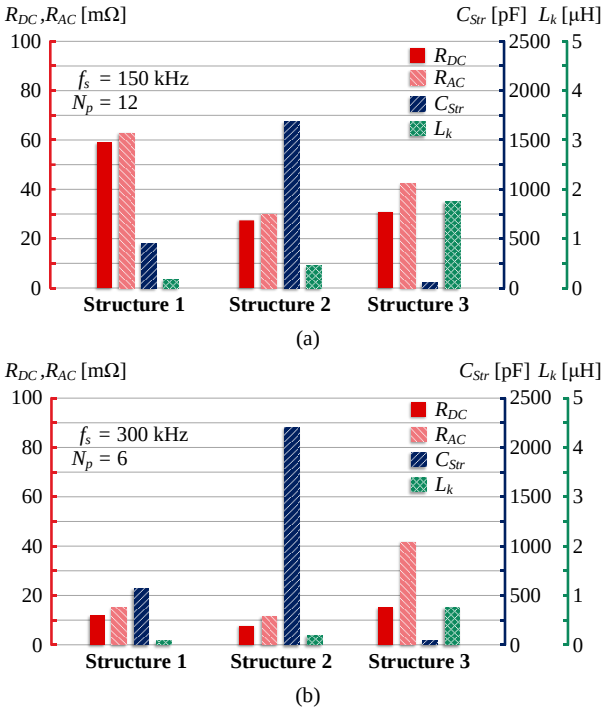

Fig. 14. Parasitic parameters of candidate winding structures from 3-D FEA simulation. (a) At f_s = 150 kHz. (b) At f_s = 300 kHz.

stray capacitance, and leakage inductance are presented. For the selected winding structure, a customized planar core is designed while taking losses and volume into account.

A. Winding Structure Comparison

The candidate winding structures are implemented on a transformer with the specifications presented in Table II. Fig. 13(a) shows the concept of the proposed PCB winding structure. Four PCBs are stacked and connected in parallel to utilize the window area of the core to utilize the whole window area so that the winding DC resistance can be minimized. The layers in each PCB are arranged with an interleaving technique to minimize the AC resistance. In Fig. 13(b), the proposed Litz wire winding concept is shown. The Litz wire consists of 200 strands with each strand having a diameter of 0.12 mm. The interleaving arrangement is also implemented in this case to minimize the AC resistance. All the winding parameters are obtained by performing 3-D FEA simulations on the candidate structures using Ansys Maxwell.

Fig. 14(a) shows the comparison of the parasitic parameters of the three candidate winding structures at f_s =150 kHz. Structure 1 (4 layers PCB) has the highest DC resistance among the other structures. By increasing the number of PCB layers, the winding DC resistance can be reduced as observed in Structure 2 (8 layers PCB), where the DC resistance is half of that in Structure 1. However, as the number of layers is increased, the overlapping area between layers is also increased, which results in high winding stray capacitance (C_{Str}). As an alternative to the PCB winding structure, the Litz wire

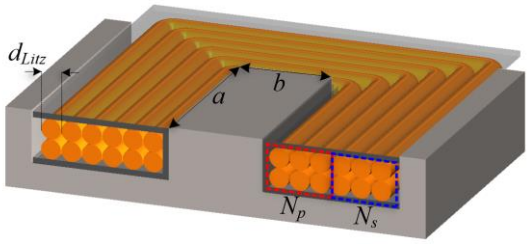

Fig. 15. Optimization variables of planar transformer with Litz wire winding.

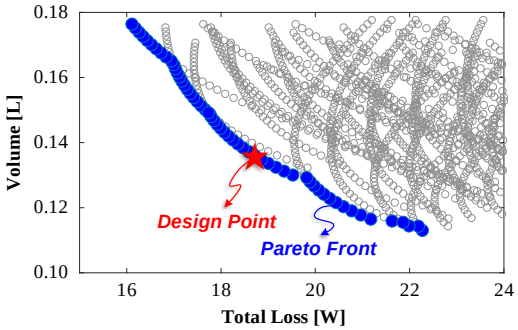

Fig. 16. Selected design point from the optimization solutions based on the Pareto Front.

TABLE II
TRANSFORMER SPECIFICATIONS

Item	Value
Core material	Customized EE, Ferrite PL-17YH SAMWHA ELECTRONICS
Peak voltage	679 V
Winding RMS current	11.4 A
Duty cycle (d_p)	50%
Switching frequency (f_s)	150 kHz

TABLE III
TRANSFORMER DESIGN AND OPTIMIZATION RESULT

Item	Values
Number of turns (N_p:N_s)	12:12
Litz wire type	0.12 mm / 200 strands
Core cross sectional area	560 mm^2
Maximum flux density (B_{max})	163 mT

This article has been accepted for publication in a future issue of this journal, but has not been fully edited. Content may change prior to final publication. Citation information: DOI 10.1109/TPEL.2021.3127010, IEEE Transactions on Power Electronics

TABLE IV
PROTOTYPE SPECIFICATIONS OF THE PROPOSED EV CHARGER

Item	Values
Rated power	11 kW (3.7 kW × 3EA)
Grid voltage	3Φ: 400 V (50 Hz), 380 V (50 Hz) 1Φ: 220 V(50 Hz), 230 V (50 Hz), 240 V (60 Hz)
Battery voltage (V_B)	460-800 V
Switching frequency (f_s)	150 kHz
Power density	5.25 kW/L (517 × 225 ×18 mm)

TABLE V
SYSTEM PARAMETERS OF THE PROPOSED EV CHARGER

Item	Values
Grid inductor (L_{g1}, L_{g2})	30 μH
Series inductor (L_{S1}, L_{S2})	20 μH
Switches (S_1-S_{10})	NVBG020N120SC1
Power decoupling cap. (C_{pd})	75.2 μF, [0.47 μF MLCC]×160
Filter cap. (C_o)	20 μF, [10 μF film cap.]×2
Clamping cap. (C_c)	1.6 μF, [0.1 μF MLCC]×16

(Structure 3) can be used. Although the AC to DC resistance ratio is higher than that of the PCB winding structure, the Litz wire structure has better DC resistance. Litz wire structure also has much lower winding stray capacitance since there is a larger isolation distance between the windings.

As shown in Fig. 14(b), the candidate winding structures are also simulated at f_s = 300 kHz where the number of turns can be reduced by half of that at f_s = 150 kHz to maintain the same core maximum flux density. Since the number of turns is reduced, all structures can achieve lower DC resistance. In terms of winding stray capacitance, Structure 2 remains the highest among the other structures. Meanwhile, in Structure 3, the AC resistance dominates the DC resistance due to the increased frequency. At f_s = 300 kHz, it is reasonable to use Structure 1 since the winding loss can be minimized, although the stray capacitance remains larger than Structure 3.

Considering all the aspects in the comparison and the given specifications, Structure 3 (Litz wire structure) is selected in this paper. At the frequency range where many turns are required, the Litz wire structure has better performance than the PCB winding structure in terms of winding DC resistance and stray capacitance. However, at a higher frequency, say 300 kHz, Litz wire may suffer from a large eddy current effect that dominates the overall winding loss. Therefore, in this case, the PCB winding structure is recommended.

B. Design and Optimization of Planar Transformer

As the transformer contributes to a large portion of the converter footprint, a proper design methodology to achieve high efficiency and high power density is important. In this section, an optimization process for the planar transformer with Litz wire is presented. The optimization objective is to select a design point based on the tradeoff between transformer volume and losses [40].

As shown in Fig 15, the free variables are the geometrical parameters *a* and *b*, whose product is the core cross-section area, number of primary turns N_p, and the wire diameter d_{Litz} which

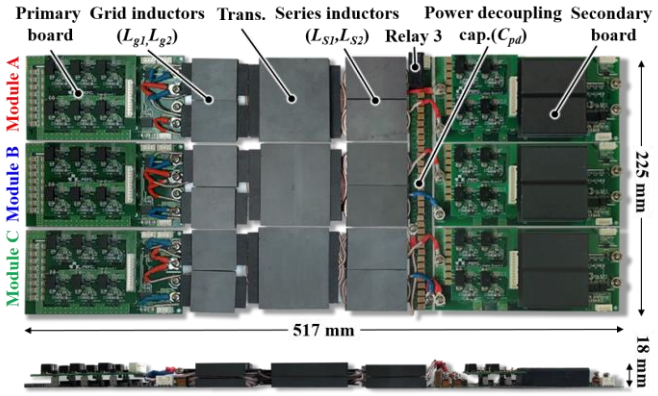

Fig. 17. Prototype of the proposed 11 kW EV charger (5.25 kW/L).

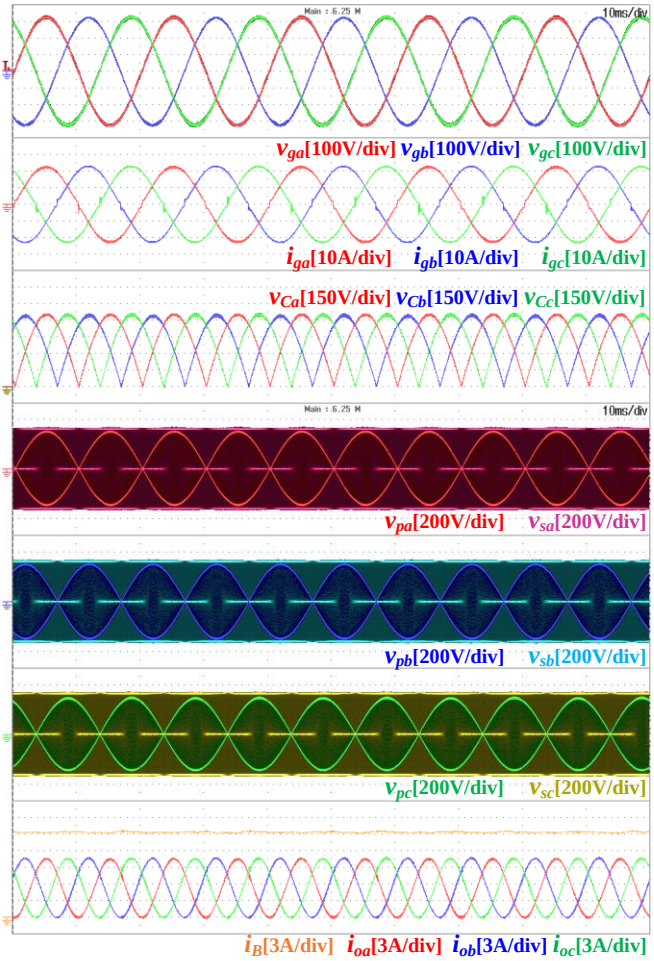

Fig. 18. Experimental waveforms under balanced three-phase grid voltage at full load.

depends on the selected Litz wire type from a given database. The variables are swept within a defined range to obtain all the transformer parameters. The obtained solutions are plotted on the losses vs volume graph, as shown in Fig 16. From these solutions, a Pareto front line that minimizes both volume and total losses can be generated, and a design point can be selected. The design results of the transformer are shown in Table III.

This article has been accepted for publication in a future issue of this journal, but has not been fully edited. Content may change prior to final publication. Citation information: DOI 10.1109/TPEL.2021.3127010, IEEE Transactions on Power Electronics

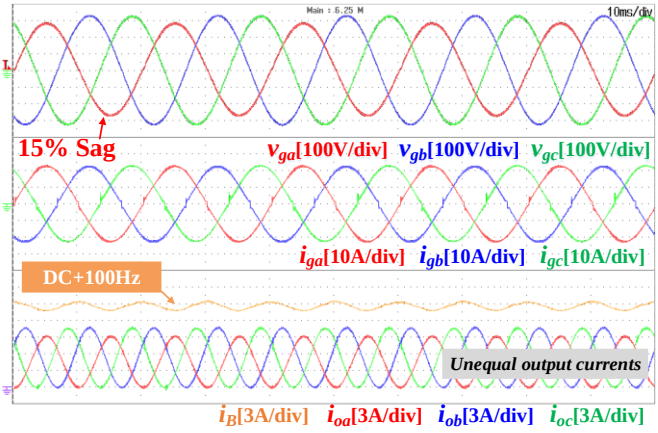

(a)

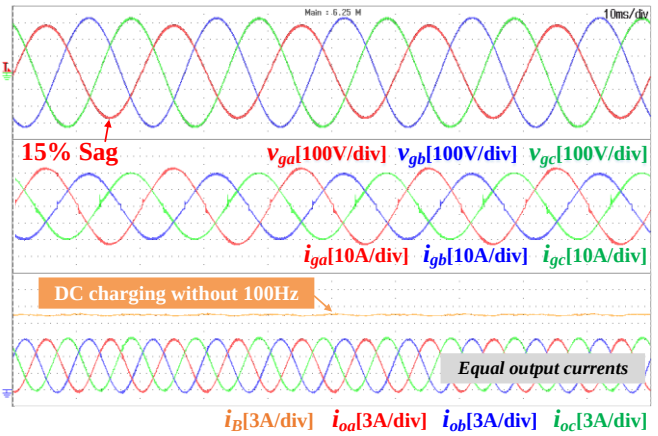

(b)

Fig. 19. Experimental waveforms under unbalanced voltage sag (v_{ga}=0.85 pu). (a) without the proposed output current balancing control. (b) with the proposed output current balancing control.

IV. Experiment Results

In order to verify the performance of the proposed single- and three-phase compatible modular EV charger, a 11 kW (3.7 kW×3 modules) laboratory prototype was built according to the specifications and system parameters given in Table IV and Table V, respectively. The proposed converter shown in Fig. 17 achieved a volumetric power density of 5.25 kW/L.

For a balanced three-phase grid voltage, Fig. 18 shows the experimental waveforms of the proposed EV charger at full load. The power factor of the three-phase grid current is close to unity. The voltage across the clamping capacitors is twice the rectified grid voltage. Since the voltages across the high frequency transformers do not include low-frequency components, lightweight HF transformers are used. The output currents of the three modules $i_{o(a,b,c)}$ mainly include DC and second harmonic components and have the same shape with 120° phase shift. Therefore, the sum of the three output currents results in DC battery current. Fig. 19 shows the effectiveness of the proposed balancing control for maintaining DC charging current. Without the proposed balancing control, the unbalanced grid of sagged phase *'a'* by 15% introduces the low-frequency component in the battery current due to the unequal power delivered by the three modules, as shown in Fig. 19(a). With the proposed balancing control, equal power is delivered by the three modules.

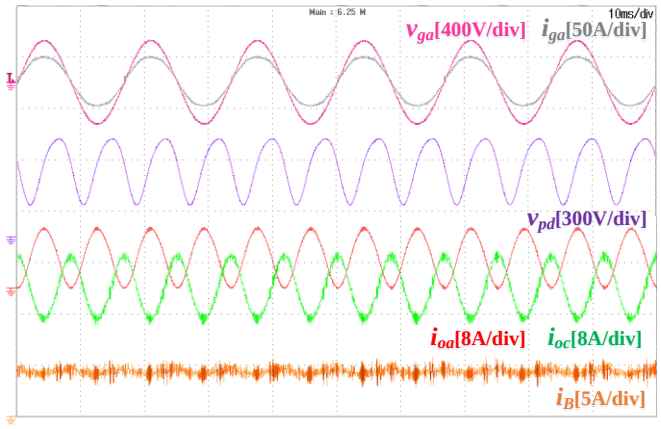

Fig. 20. Experimental waveforms for single-phase grid at 3.7 kW.

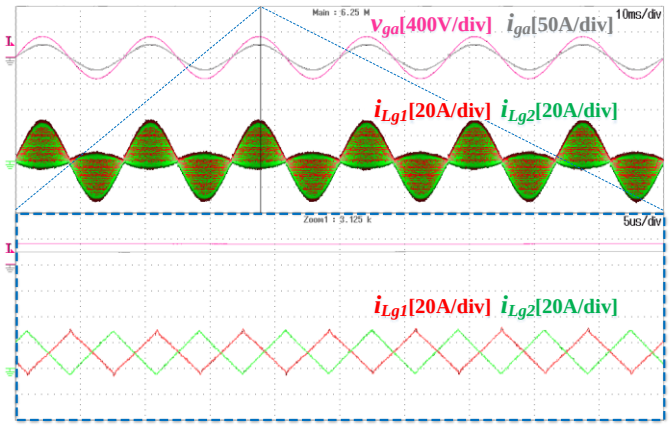

Fig. 21. Experimental waveforms showing input inductor currents and grid current.

Hence, the second-harmonic is eliminated, and DC charging current is ensured, as shown in Fig 19(b).

Fig. 20 shows the experimental waveforms of the proposed EV charger at 3.7 kW for a single-phase grid. While the charging power is delivered by *Module A*, *Module C* operates as the integrated power decoupling circuit. Output current i_{oa} of *Module A* pulsates at twice the grid-frequency. The second-harmonic current i_{oc} drawn by *Module C* cancels the second-harmonic components of i_{oa}, thereby charging the battery with DC current.

Fig. 21 shows experimental waveforms showing input inductor currents and grid current. The grid current is high frequency ripple-free due to the fixed 50% duty-cycle of the two interleaving legs.

During the positive (negative) half-cycle, switch S_3 (S_4) operates as synchronous rectifier and its ZVS turn-on is inherently achieved. The waveforms drain-source voltage v_{ds} and gating signal v_{gs} of the switches S_3, S_4, S_7 and S_8 at grid voltage phase angles of 50° and 90° in Fig. 22 verify the ZVS turn-on of S_3 and S_4. The switching loss of S_1 and S_2 is negligible in practice since two switches commutate at the grid frequency.

Fig. 23 shows ZVS range according to battery voltage range when V_g = 230 V. As shown in Fig. 23(a), the ZVS turn-on of S_4 (representing primary-side switches) can always be achieved. When the battery voltage is 460 V which is the worst case

This article has been accepted for publication in a future issue of this journal, but has not been fully edited. Content may change prior to final publication. Citation information: DOI 10.1109/TPEL.2021.3127010, IEEE Transactions on Power Electronics

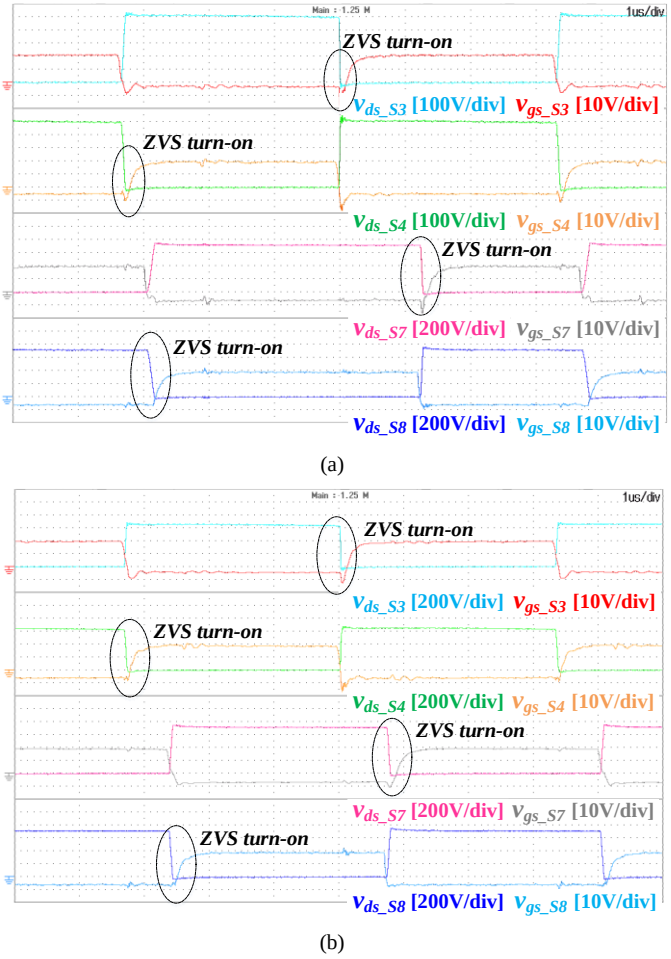

Fig. 22. Experimental waveforms showing ZVS turn on of switches S_3, S_4, S_7 and S_8. (a) at grid voltage phase angle of 50°. (b) at grid voltage phase angle of 90°.

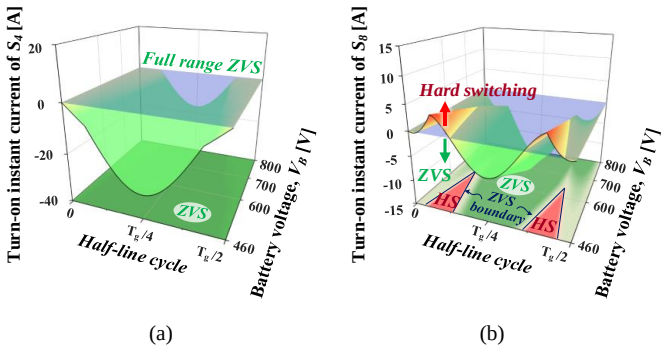

Fig. 23. ZVS range according to battery voltage when V_g = 230 V. (a) primary –side switch S_4. (b) secondary-side switch S_8.

operation, ZVS turn-on of S_8 (representing secondary-side switches) is achieved except low grid voltage region, as shown in Fig. 23(b). However, ZVS turn-on of S_8 is always achieved for battery voltage over 630 V. Therefore, the proposed EV charger is able to achieve ZVS turn-on under wide grid and battery voltage ranges during the CC-CV charging profile.

The measured efficiencies of the proposed EV charger for different battery voltages are shown in Fig. 24. For three-phase charging a peak efficiency of 97.01% is achieved at battery

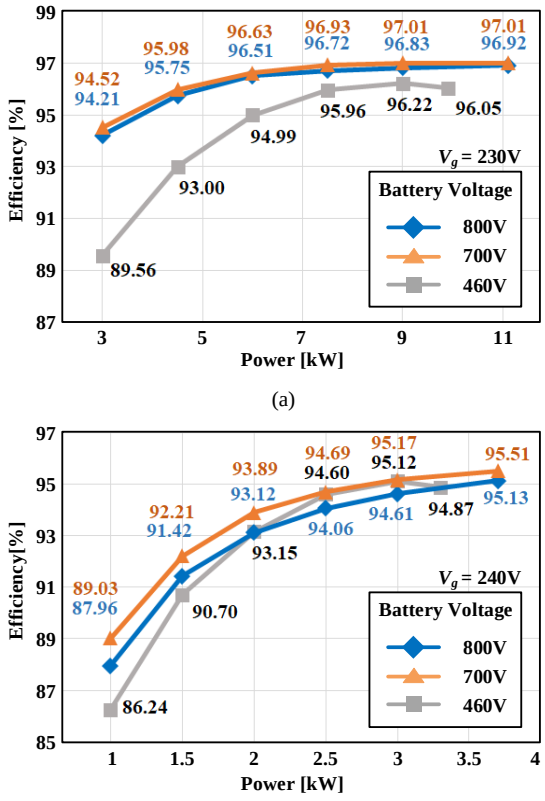

Fig. 24. Efficiencies of the proposed EV charger (measured by Yokogawa WT3000). (a) for three-phase grid. (b) for single-phase grid.

voltage of 700 V as shown in Fig. 22(a). The peak efficiency for single-phase charging is 95.51% at full load for battery voltage of 700 V as shown in Fig. 22(b). Compared with the efficiency of the three-phase charging, that of the single-phase charging is dropped by 1.5% due to the operation of the power decoupling circuit.

In Table VI, the proposed EV charger is compared to single- and three-phase compatible EV chargers introduced in [20], [32], and [41]. The proposed EV charger and the charger in [32] are the modular single-stage topology, whereas the topologies in [20] and [41] are the non-modular two-stage. It is worthy to mention that integrating power decoupling circuits in the proposed EV charger and [20] further decreases the circuits complexity and components count. The proposed EV charger achieves ZVS turn-on of all switches using simple control method with one control variable. However, the whole range ZVS of the charger in [32] is achieved by introducing three control variables with varying switching frequency (150-500 kHz). In topology standpoint, the switch count of the proposed EV charger is 30 while the switch-count of the charger in [32] is 36. However, in [32], for a 22 kW charger, the actual total number of GaN HEMT is 96 except unfolding bridges since each high-frequency switch uses four paralleled GaN HEMT. The proposed EV charger has similar switch utilization factor, transformer VA rating, and series inductor VA rating compared to the charger in [32]. However, it seems that the series inductor of the charger in [32] was integrated into the transformer. The

This article has been accepted for publication in a future issue of this journal, but has not been fully edited. Content may change prior to final publication. Citation information: DOI 10.1109/TPEL.2021.3127010, IEEE Transactions on Power Electronics

TABLE VI
COMPARISON OF THE PROPOSED EV CHARGER WITH OTHER SINGLE- AND THREE-PHASE COMPATIBLE TOPOLGIES.

		Proposed EV charger	[32]*	[20]*	[41]
Structure		Modular Single-stage	Modular single-stage	Non-modular two-stage	Non-modular two-stage
Topology	3-phase	Totem-pole based current-fed DAB	Indirect matrix based voltage-fed DAB	Six-switch boost PFC + Two DCX DC-DC	Six-switch boost PFC + Two DC-DC in series
	1-phase			Full-bridge PFC + Two DCX DC-DC	3-phase totem-pole PFC + Two DC-DC in parallel
Second-harmonic storage		**Film cap. with integrated PD circuit**	Film cap. with additional PD circuit	Film cap. with integrated PD circuit	Electrolytic capacitors
Controller		**Simple**	Complex	Simple	Simple
Soft switching characteristic		**ZVS turn-on**	ZVS turn-on	PFC stage: Hard switched DC-DC stage: ZVS turn-on	PFC stage: Hard switched DC-DC stage: ZVS turn-on
Power rating		3Φ: 11 kW 1Φ: 7.4 kW	3Φ: 22 kW 1Φ: ?	3Φ: 22 kW 1Φ: 7.36 kW	3Φ: 22 kW 1Φ: 19.2 kW
Grid voltage		3Φ: 380 / 400 V 1Φ: 220 / 230 / 240 V	3Φ: 360 V 1Φ: 208 V	3Φ: 400 V 1Φ: 230 V	3Φ: 400 V 1Φ: 230 / 240 V
Battery voltage		460-800 V	200-450 V	200-450 V	?
Switching freq.		150 kHz	150-500 kHz	PFC stage: 36 kHz DC-DC stage: ?	PFC stage: 48 kHz DC-DC stage: ?
Switch count in topology standpoint		30 SiC Mosfet	24 GaN HEMT 12 Si Mosfet (unfolding bridge)	PFC stage: 6 Si Mosfet DC-DC stage: 16 Si Mosfet	PFC stage: 6 SiC Mosfet +2 Si Diode DC-DC stage: ?
Switch utilization factor		0.0204	0.0216	?	?
Transformer VA rating		1.15 pu	1.10 pu	?	?
Series inductor VA rating		1.16 pu	1.21 pu	?	?
Power density		**4.15 kW/L (w/ air-cooled heatsink) 5.25 kW/L (w/o heatsink)_**	3.3 kW/L (Heatsink was not specified)	2.04 kW/L (water-cooled heatsink)	**?**
Peak efficiency		97.01%	> 97%	94.0%	?

* Company made prototype (Commercialized topology)
? No information is provied in the reference.

$$\textit{Switch utilization factor} = \frac{P_{out}}{\sum_{j=1}^{N} V_{S\,peak(j)} \times I_{S\,peak(j)}}$$

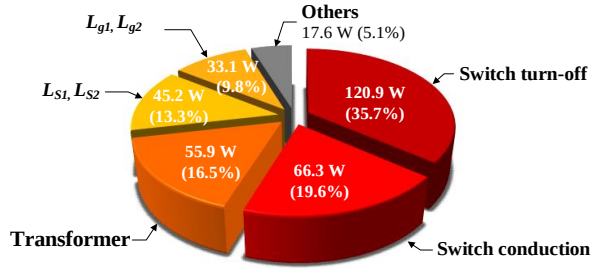

(a)

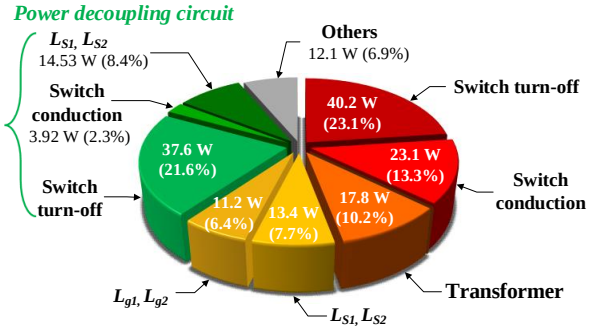

(b)

Fig. 25. Loss breakdown of the proposed EV charger. (a) for three-phase grid (V_g = 400 V, V_B = 700 V, and P_{out} = 11 kW). (b) for single-phase grid (V_g = 240 V, V_B = 700 V, and P_{out} = 3.7 kW).

PFC stage in non-modular two-stage EV chargers in [20] and [41] is operated with limited switching frequency due to the hard switching characteristic. Therefore, achieving high power density is a crucial task. The high power density offered by the proposed EV charger is due to the low profile attributed to the absence of electrolytic capacitors and the optimization of the magnetic components. Since the proposed EV charger is a single-stage bridgeless type achieving wide ZVS range, conduction and switching losses are significantly reduced, thereby achieving high efficiency.

Fig. 25 represents the loss breakdown of the proposed EV charger. For three-phase grid, about 55.3% of the total losses occur in the semiconductors, as shown in Fig. 25(a). Core and winding losses in the magnetic components including the transformer, input inductors (L_{g1} and L_{g2}), and series inductors (L_{S1} and L_{S2}) account for 39.6%. For single-phase grid, as shown in Fig. 25(b), semiconductors and magnetic losses are 36.4% and 24.3% of the total loss, respectively. Unlike the three-phase grid, *Module C* operating as a power decoupling circuit incurs additional losses with a potion of 32.3% of the total losses.

V. CONCLUSION

In this paper, a modular single-stage electrolytic capacitor-less OBC that is compatible with single- and three-phase grid is proposed. The proposed integrated power decoupling method enables the proposed EV charger to provide DC battery charging

current under single-phase grid without the use of an additional circuit. With the proposed balancing control, charging power was equally distributed among the three modules, thereby eliminating the second-harmonic ripple at the battery side and ensuring a pure DC charging current. The low profile of 18 mm is achieved owing to the optimized Litz-winding planar magnetic as well as the elimination of the electrolytic capacitors, resulting in power density of 5.25 kW/L. The ZVS turn-on for all switching devices is maintained, leading to high efficiency over wide voltage and load range. The proposed single-stage electrolytic capacitor-less EV charger could be a viable solution for high power density and high reliable OBC.

REFERENCES

[1] U.S. DRIVE Department of Energy, “Electrical and electronics technical t eam roadmap”, Oct.-2017. [Online]. Available: https://www.energy.gov/s ites/prod/files/2017/11/f39/EETT%20Roadmap%2010-27-17.pdf. [Accessed: 10-Mar.-2021].

[2] A. Braham, A. Lahyani, P. Venet and N. Rejeb, "Recent Developments in Fault Detection and Power Loss Estimation of Electrolytic Capacitors," i n *IEEE Transactions on Power Electronics*, vol. 25, no. 1, pp. 33-43, Jan. 2010, doi: 10.1109/TPEL.2009.2026749.

[3] M. Yilmaz and P. T. Krein, "Review of Battery Charger Topologies, Char ging Power Levels, and Infrastructure for Plug-In Electric and Hybrid Ve hicles," in *IEEE Transactions on Power Electronics*, vol. 28, no. 5, pp. 21 51-2169, May 2013, doi: 10.1109/TPEL.2012.2212917.

[4] Mark Kane, “France Expanded Its Charging Infrastructure By 15% This Year”,28-Dec.-2019.[Online].Available: https://insideevs.com/news/389 536/france-expanded-charging-infrastructure/. [Accessed: 10-Mar.-2021].

[5] Mark Kane, “2020 Hyundai Kona Electric To Get 11 kW 3-Phase On-Board Charger”, 08-May-2019. [Online]. Available: https://insideevs .com/news/348498/hyundai-kona-electric-11-kw-charger/. [Accessed: 10-Mar.-2021].

[6] S. Choi, "Power Converter Technology for xEV-Current status and Challe nge," Presentation at the Plenary Session, *2020 IEEE 9th International Power Electronics and Motion Control Conference (IPEMC2020-ECCE Asia)*, Nanjing, China, 2020.

[7] C. Liu *et al*., "High-Efficiency Hybrid Full-Bridge–Half-Bridge Converter With Shared ZVS Lagging Leg and Dual Outputs in Series," in *IEEE Transactions on Power Electronics*, vol. 28, no. 2, pp. 849-861, Feb. 2013, doi: 10.1109/TPEL.2012.2205019.

[8] J. Schmenger, S. Endres, S. Zeltner and M. März, "A 22 kW on-board charger for automotive applications based on a modular design," *2014 IEEE Conference on Energy Conversion (CENCON)*, Johor Bahru, Malaysia, 2014, pp. 1-6, doi: 10.1109/CENCON.2014.6967467.

[9] G. Yang, E. Draugedalen, T. Sorsdahl, H. Liu and R. Lindseth, "Design of High Efficiency High Power Density 10.5kW Three Phase On-board-charger for Electric/hybrid Vehicles," *PCIM Europe 2016; International Exhibition and Conference for Power Electronics, Intelligent Motion, Renewable Energy and Energy Management*, Nuremberg, Germany, 2016, pp. 1-7.

[10] D. Cesiel and C. Zhu, "A Closer Look at the On-Board Charger: The development of the second-generation module for the Chevrolet Volt," in *IEEE Electrification Magazine*, vol. 5, no. 1, pp. 36-42, March 2017, doi: 10.1109/MELE.2016.2644265.

[11] G. Liu, Y. Jang, M. M. Jovanović and J. Q. Zhang, "Implementation of a 3.3-kW DC–DC Converter for EV On-Board Charger Employing the Series-Resonant Converter With Reduced-Frequency-Range Control," in *IEEE Transactions on Power Electronics*, vol. 32, no. 6, pp. 4168-4184, June 2017, doi: 10.1109/TPEL.2016.2598173.

[12] Z. Liu, B. Li, F. C. Lee and Q. Li, "High-Efficiency High-Density Critical Mode Rectifier/Inverter for WBG-Device-Based On-Board Charger," in *IEEE Transactions on Industrial Electronics*, vol. 64, no. 11, pp. 9114-9123, Nov. 2017, doi: 10.1109/TIE.2017.2716873.

[13] B. Li, Q. Li, F. C. Lee, Z. Liu and Y. Yang, "A High-Efficiency High-Density Wide-Bandgap Device-Based Bidirectional On-Board Charger," in *IEEE Journal of Emerging and Selected Topics in Power Electronics*, vol. 6, no. 3, pp. 1627-1636, Sept. 2018, doi: 10.1109/JESTPE.2018 .2845846.

[14] B. Li, Q. Li and F. C. Lee, "High-Frequency PCB Winding Transformer With Integrated Inductors for a Bi-Directional Resonant Converter," in *IEEE Transactions on Power Electronics*, vol. 34, no. 7, pp. 6123-6135, July 2019, doi: 10.1109/TPEL.2018.2874806.

[15] H. Li, Z. Zhang, S. Wang, J. Tang, X. Ren and Q. Chen, "A 300-kHz 6.6-kW SiC Bidirectional LLC Onboard Charger," in *IEEE Transactions on Industrial Electronics*, vol. 67, no. 2, pp. 1435-1445, Feb. 2020, doi: 10.1109/TIE.2019.2910048.

[16] D. Yang, B. Duan, W. Ding, C. Zhang, J. Song and H. Bai, "Turn-Off Delay-Controlled Bidirectional DC–DC Resonant Converter With Wide Gain Range and High Efficiency," in *IEEE Transactions on Transportation Electrification*, vol. 6, no. 1, pp. 118-130, March 2020, doi: 10.1109/TTE.2020.2965326.

[17] Y. Yan, H. Bai, A. Foote and W. Wang, "Securing Full-Power-Range Zero-Voltage Switching in Both Steady-State and Transient Operations for a Dual-Active-Bridge-Based Bidirectional Electric Vehicle Charger," in *IEEE Transactions on Power Electronics*, vol. 35, no. 7, pp. 7506-7519, July 2020,doi: 10.1109/TPEL.2019.2955896.

[18] R. Kondo, P. Schülting, A. H. Wienhausen and R. W. De Doncker, "An Automated Component-Based Hardware Design of a Three-Phase Dual-Active Bridge Converter for a Bidirectional On-Board Charger," *2020 IEEE Energy Conversion Congress and Exposition (ECCE)*, Detroit, MI, USA, 2020, pp. 850-857, doi: 10.1109/ECCE44975.2020.9236190.

[19] S. Zeljkovic, R. Vuletic, A. Miller and A. Denais, "Control of SiC-based dual active bridge in high power three phase on-board charger of EVs," *2015 International Conference on Electrical Systems for Aircraft, Railway, Ship Propulsion and Road Vehicles (ESARS)*, Aachen, Germany, 2015, pp. 1-6, doi: 10.1109/ESARS.2015.7101454.

[20] K. Stengert, "On-board 22 kW fast charger “NLG6”," *2013 World Electric Vehicle Symposium and Exhibition (EVS27)*, Barcelona, Spain, 2013, pp. 1-11, doi: 10.1109/EVS.2013.6914854.

[21] H. Zhao, Y. Shen, W. Ying, S. S. Ghosh, M. R. Ahmed and T. Long, "A Single- and Three-Phase Grid Compatible Converter for Electric Vehicle On-Board Chargers," in *IEEE Transactions on Power Electronics*, vol. 35, no. 7, pp. 7545-7562, July 2020, doi: 10.1109/TPEL.2019.2956653.

[22] L. Xue, Z. Shen, D. Boroyevich, P. Mattavelli and D. Diaz, "Dual Active Bridge-Based Battery Charger for Plug-in Hybrid Electric Vehicle With Charging Current Containing Low Frequency Ripple," in *IEEE Transactions on Power Electronics*, vol. 30, no. 12, pp. 7299-7307, Dec. 2015, doi: 10.1109/TPEL.2015.2413815.

[23] S. Li, J. Deng and C. C. Mi, "Single-Stage Resonant Battery Charger With Inherent Power Factor Correction for Electric Vehicles," in *IEEE Transactions on Vehicular Technology*, vol. 62, no. 9, pp. 4336-4344, Nov. 2013, doi: 10.1109/TVT.2013.2265704.

[24] B. Kim, M. Kim and S. Choi, "A reduced component count single-stage electrolytic capacitor-less battery charger with sinusoidal charging," *2017 IEEE 3rd International Future Energy Electronics Conference and ECCE Asia (IFEEC 2017 - ECCE Asia)*, Kaohsiung, 2017, pp. 242-246, doi: 10.1109/IFEEC.2017.7992044.

[25] J. Lu *et al*., "Applying Variable-Switching-Frequency Variable-Phase-Shift Control and E-Mode GaN HEMTs to an Indirect Matrix Converter-Based EV Battery Charger," in *IEEE Transactions on Transportation Electrification*, vol. 3, no. 3, pp. 554-564, Sept. 2017, doi: 10.1109/TTE.2017.2723944.

[26] A. Taylor, J. Lu, L. Zhu, K. Bai, M. McAmmond, and A. Brown, “Comparison of SiC MOSFET-based and GaN HEMT-based high-efficiency high-power-density 7.2 /kW EV battery chargers,” *IET Power Electronics*, vol. 11, no. 11, pp. 1849–1857, 2018.

[27] H. Belkamel, H. Kim and S. Choi, "Interleaved Totem-Pole ZVS Converter Operating in CCM for Single-Stage Bidirectional AC–DC Conversion With High-Frequency Isolation," in *IEEE Transactions on Power Electronics*, vol. 36, no. 3, pp. 3486-3495, March 2021, doi: 10.1109/TPEL.2020.3016684.

[28] H. Belkamel, K. Hyungjin, K. Beywongwoo, Y. Shin and S. Choi, "Bi-Directional Single-Stage Interleaved Totem-Pole AC-DC Converter with High Frequency Isolation for On-Board EV Charger," *2018 IEEE Energy Conversion Congress and Exposition (ECCE)*, Portland, OR, USA, 2018, pp. 6721-6724, doi: 10.1109/ECCE.2018.8557933.

[29] F. Jauch and J. Biela, "Combined Phase-Shift and Frequency Modulation of a Dual-Active-Bridge AC–DC Converter With PFC," in *IEEE*

Transactions on Power Electronics, vol. 31, no. 12, pp. 8387-8397, Dec. 2016, doi: 10.1109/TPEL.2016.2515850.

[30] B. Eckardt, M. Wild, C. Joffe, S. Zeltner, S. Endres and M. Maerz, "Advanced Vehicle Charging Solutions Using SiC and GaN Power Devices," *PCIM Europe 2018; International Exhibition and Conference for Power Electronics, Intelligent Motion, Renewable Energy and Energy Management*, Nuremberg, Germany, 2018, pp. 1-6.

[31] L. Schrittwieser, P. Cortés, L. Fässler, D. Bortis and J. W. Kolar, "Modulation and Control of a Three-Phase Phase-Modular Isolated Matrix-Type PFC Rectifier," in *IEEE Transactions on Power Electronics*, vol. 33, no. 6, pp. 4703-4715, June 2018, doi: 10.1109/TPEL.2017 .2726342.

[32] J. Lu *et al*., "A Modular-Designed Three-Phase High-Efficiency High-Power-Density EV Battery Charger Using Dual/Triple-Phase-Shift Control," in *IEEE Transactions on Power Electronics*, vol. 33, no. 9, pp. 8091-8100, Sept. 2018, doi: 10.1109/TPEL.2017.2769661.

[33] D. Das, N. Weise, K. Basu, R. Baranwal and N. Mohan, "A Bidirectional Soft-Switched DAB-Based Single-Stage Three-Phase AC–DC Converter for V2G Application," in *IEEE Transactions on Transportation Electrification*, vol. 5, no. 1, pp. 186-199, March 2019, doi: 10.1109/TTE. 2018.2886455.

[34] L. Schrittwieser, M. Leibl and J. W. Kolar, "99% Efficient Isolated Three-Phase Matrix-Type DAB Buck–Boost PFC Rectifier," in *IEEE Transactions on Power Electronics*, vol. 35, no. 1, pp. 138-157, Jan. 2020, doi: 10.1109/TPEL.2019.2914488.

[35] H. Kim, H. Belkamel, J. Park, R. M. Hakim and S. Choi, "Modular Three-phase Single-stage Isolated AC-DC Converter for Electrolytic Capacitor-less EV DC Charging," 2020 *IEEE 9th International Power Electronics and Motion Control Conference (IPEMC2020-ECCE Asia)*, Nanjing, China, 2020, pp. 1573-1578, doi: 10.1109/IPEMC-ECCEAsia48364.2020.9368079.

[36] O. GarcÍa, P. Zumel, A. de Castro, P. Alou and J. A. Cobos, "Current Self-Balance Mechanism in Multiphase Buck Converter," in *IEEE Transactions on Power Electronics*, vol. 24, no. 6, pp. 1600-1606, June 2009, doi: 10.1109/TPEL.2009.2013859.

[37] Z. Zhang, C. Liu, M. Wang, Y. Si, Y. Liu and Q. Lei, "High-Efficiency High-Power-Density CLLC Resonant Converter With Low-Stray-Capacitance and Well-Heat-Dissipated Planar Transformer for EV On-Board Charger," in *IEEE Transactions on Power Electronics*, vol. 35, no. 10, pp. 10831-10851, Oct. 2020, doi: 10.1109/TPEL.2020.2980313.

[38] V. Leonavicius, M. Duffy, U. Boeke and S. C. O. Mathuna, "Comparison of realization techniques for PFC inductor operating in discontinuous conduction mode," in *IEEE Transactions on Power Electronics*, vol. 19, no. 2, pp. 531-541, March 2004, doi: 10.1109/TPEL.2003.823249.

[39] M. A. Saket, N. Shafiei and M. Ordonez, "LLC Converters With Planar Transformers: Issues and Mitigation," in *IEEE Transactions on Power Electronics*, vol. 32, no. 6, pp. 4524-4542, June 2017, doi: 10.1109/TPEL. 2016.2602360.

[40] A. M. Naradhipa, S. Kim, D. Yang, S. Choi, I. Yeo and Y. Lee, "Power Density Optimization of 700 kHz GaN-Based Auxiliary Power Module for Electric Vehicles," in *IEEE Transactions on Power Electronics*, vol. 36, no. 5, pp. 5610-5621, May 2021, doi: 10.1109/TPEL.2020.3026328.

[41] P. Papamanolis, F. Krismer and J. W. Kolar, "22 kW EV Battery Charger Allowing Full Power Delivery in 3-Phase as well as l-Phase Operation," *2019 10th International Conference on Power Electronics and ECCE Asia (ICPE 2019 - ECCE Asia)*, Busan, Korea (South), 2019, pp. 1-8.

[42] Choi, Se Wan. "Single-stage interleaved soft switching converter." U.S. Patent pending.

[43] Choi, Se Wan. "Three phase and single phase compatible charger." PCT Patent pending.